Hydroxyl-Stretching Region in the Raman Broad Scans on Minerals of the Vivianite Group (Vivianite, Baricite, Bobierrite, Annabergite, Erythrite)

International Journal of Sciences

Research Article Volume 13 – August 2024 (08)

Hydroxyl-Stretching Region in the Raman Broad Scans on Minerals of the Vivianite Group (Vivianite, Baricite, Bobierrite, Annabergite, Erythrite)

Amelia Carolina Sparavigna[1]

[1]Department of Applied Science and Technology, Polytechnic University of Turin, Italy

Abstract: Vivianite is a hydrated iron phosphate mineral ($Fe_3(PO_4)_2 \cdot 8H_2O$), crystallized in a monoclinic system. It is the endmember of a mineral series known as the vivianite group, where minerals have the general formula $A_3(XO_4)_2 \cdot 8H_2O$, A is a divalent metal cation and X is phosphorus P or arsenic As. Today, vivianite is attracting interest as a promising material for recovering phosphorous from wastewaters. In fact, the presence in wastewater sludges of soluble iron and phosphorus can lead to vivianite formation. As a crystal, it is a naturally occurring Van der Walls material. It can be easily characterized by means of Raman and infrared spectroscopies. Here we will consider the Raman spectroscopy, precisely that related to the hydroxyl-stretching region. We will propose the deconvolutions in q-Gaussian functions of spectra from RRUFF database, comparing the obtained results with those available from literature. Besides vivianite, we will consider also baricite, bobierrite, annabergite and erythrite, other members of the vivianite group. About the hydroxyl-stretching region and the use of q-Gaussians, we take the chance to continue a discussion regarding the Raman spectroscopy of water, discussion that we started in March 2024.

Keywords: Vivianite Group Minerals, Vivianite, Baricite, Bobierrite, Annabergite, Erythrite, Raman Spectroscopy, Q-Gaussian Functions, Tsallis Statistics, Hydroxyl-Stretching Raman Region, OH-Stretching Raman Region, Biochar, Wastewater Treatment, Fertilizers, Minerals On Mars, Minerals On Moon

Introduction

Here we consider the Raman broad scans on minerals of the vivianite group, scans which are published in the RRUFF database. The minerals of the vivianite group are of the general formula $(A^{2+})_3(XO_4)_2 \cdot 8H_2O$. In this formula, A^{2+} can be Co, Fe, Mg, Ni, Zn and X can be As or P (Frost et al., 2002). In RRUFF database, we can find vivianite, baricite, bobierrite and other minerals of the group. Of the Raman broad scans, we will consider the range between 2000 and 4000 cm^{-1}, which contains the hydroxyl-stretching region (for water, from 2800 to 3800 cm^{-1}), that is the OH-stretching band. We have already considered this region when we studied the Raman spectroscopy of water; we proposed specifically the decomposition of this large OH-stretching band in components with the q-Gaussian profile. Being the q-parameter of q-Gaussian functions related to the correlation time of stochastic Kubo modelling of fluctuations, we stressed the use of this parameter to characterize the local environments of O-H bonds. We further discussed the OH-stretching band of ice, to understand how the decomposition in q-Gaussians changes in the number of components and values of q-parameters. Here, we will apply the same approach used for water, that is a decomposition of the spectrum in q-Gaussian components, to the scans on vivianite. We will compare the results obtained by means of q-Gaussians with the results given by literature. Baricite, bobierrite, annabergite and erythrite are also studied.

Before addressing the Raman spectroscopy of vivianite, let us remember some general literature about this material. Moreover, let us stress that vivianite is formed "in specific geological processes and conditions, and it is typically found in particular environments" (geologyscience.com). About formation of the mineral, this web site notes that "vivianite often forms in environments where anaerobic (low-oxygen) conditions prevail, such as in the sediment at the bottom of swamps, bogs, marshes, or other waterlogged areas. Bacteria play a significant role in the formation of vivianite by reducing iron ions (Fe^{3+}) to the ferrous state (Fe^{2+}), making them available for reaction with phosphate ions". The presence of phosphate ions is fundamental for vivianite creation, such as water. These phosphate ions are coming from organic materials. "Vivianite forms in iron-rich environments because it requires ferrous iron (Fe^{2+}) for its crystal structure. Iron-rich sediments, often associated with iron ore deposits, can provide the necessary iron for vivianite formation". Geologyscience.com gives the following locations to find vivianite: swamps and bogs, wetlands and marshes, mining areas. Moreover, vivianite can be found associated with minerals and rocks: pyrite, goethite, limonite. In Italy, we can find vivianite from Montoso Quarries, Bagnolo Piemonte, Cuneo.

Literature about vivianite

In Frisenda et al., 2020, we can find discussed the naturally occurring van der Waals materials. Among

Published at: http://www.ijsciences.com/pub/issue/2024-08/
DOI: 10.18483/ijSci.2787; Online ISSN: 2305-3925; Print ISSN: 2410-4477

Amelia Carolina Sparavigna (Correspondence)
+

the phosphates, Frisenda and coworkers described the vivianite as "a hydrated iron phosphate with an *approximate* formula $Fe^{2+}Fe_2^{2+}(PO_4)_2 \cdot 8H_2O$". The researchers are also proposing a picture of the crystal lattice. "Bulk vivianite has been used as natural electron donor to effectively dechlorinate a variety of chlorinated organics, the principal and most frequently found contaminants in soil and groundwater that generates significant environmental problems". For instance, Jeon et al., 2015, proposed theoretical and experimental research about the dechlorination of carbon tetrachloride on a vivianite surface. Frisenda and coworkers also provide references about the band gap of vivianite as "an indirect band gap in the range of ~3.3–4.6 eV and a paramagnetic ground state" (Li et al., 2016, Pinto et al., 2014).

About vivianite we have a large literature on its natural occurrences in different environmental conditions. Rothe and coworkers, 2016, proposed a review of "the nature, occurrence and environmental relevance of" the mineral. As explained by Silva et al., 2024, vivianite is a "mineral that can be associated with biogeochemical processes. The mineral is found in freshwater and marine systems as a biogenic product while it can undergo oxidation caused by the action of neutrophilic or photoautotrophic microorganisms" (Silva et al., mentioning Rothe et al., 2016, Miot et al., 2009, Kappler & Newman, 2004). For a recent review, see Paskin, 2024.

In industrial environment, vivianite can be found in wastewater treatment plants. As noted in Prot et al., 2021, the presence in wastewater sludge of soluble iron and phosphorus can lead to vivianite formation, that is, to the "vivianite scaling" problem. "Vivianite scaling is widely occurring in wastewater treatment plant even though it is rarely reported". "Iron reduction appears to be the cause of vivianite scaling in anaerobic equipment. … Solubility of vivianite decreases when T>32 °C, favoring scaling in heat exchangers. … [Vivianite] is usually present as a hard and blue deposit that can also be brown or black depending on its composition and location" (Prot et al., 2021). However, vivianite can be turned into an important resource; this can happen by means of methods for the phosphorus recovery (Yang et al., 2023).

In Wu et al., 2019, we can find a review of "potentials and challenges of phosphorus recovery as vivianite from wastewater". "Due to the shortage of phosphorus resources and the limitations of existing phosphorus recovery methods, phosphorus recovery in the form of vivianite has attracted considerable attention with its natural ubiquity, easy accessibility and foreseeable economic value". Wu and coworkers are proposing a review which summarizes the chemistry of vivianite. Then, the phosphorus recovery as vivianite has been comprehensively evaluated, "from the prospects of economic value and engineering feasibility". According to Wu and coworkers, in 2019 there was an "insufficient understanding on vivianite recovery in wastewater/sludge", which was decelerating "the development and exploration of such advanced approach" (Wu et al., 2019).

Zhang et al., 2022, note that the development of "feasible techniques to recover phosphorous (P) from wastewater and sewage sludge is urgent work to meet the huge demand for P resources and wastewater/sludge management. Recently, recovering P as value-added vivianite has aroused great interest due to the convenient process operation, high recovery efficiency, and wide applications of vivianite". Advanced technologies are "including ion exchange, electrodialysis, capacitive de-ionization, membrane bioreactor, anaerobic fermentation, chemical precipitation, electrochemical crystallization, biomineralization, and anaerobic digestion" as summarized by Zhang and coworkers.

Other literature on this subject, that is the sewage and wastewater treatment, are Wilfert et al., 2016, 2018, Liu et al., 2018, Wang et al., 2018. Zhao et al., 2024, propose an "efficient phosphorus recovery from waste activated sludge", by means of a "pretreatment with natural deep eutectic solvent and recovery as vivianite". Lu et al., 2024, study the "anaerobic recovery of vivianite from waste-activated sludge through combined sludge pre-fermentation and agroforestry biomass-based biochar". "If enough iron is present in the sludge after anaerobic digestion, 70–90% of total phosphorus (P) can be bound in vivianite. Based on its paramagnetism and inspired by technologies used in the mining industry, a magnetic separation procedure has been developed" (Prot et al., 2019). Priambodo et al., 2017, proposed the phosphorus recovery as vivianite by means of the treatment of wastewater from the production of thin film transistor-liquid crystal displays. Chen et al., 2023, propose a "study on anaerobic phosphorus release from pig manure", recovered "by vivianite method". Chen and coworkers established a recovery route which is combining "the electrochemical method with the vivianite method using sacrificial iron anode".

Lu and coworkers stress that phosphorus "plays a crucial role in the growth of plants and crops", "but the utilization of phosphorus resources faces two significant challenges". First, "under natural conditions, phosphorus ore is non-renewable". Therefore, according to Lu and coworkers, we are close to a future "phosphorus crisis" in human society. The other challenge is that, since "phosphorus is easily discharged into the water

through human production and daily life", we are facing the problem of "phosphorus pollution" (see Lu et al, and references therein). Lu and coworkers are providing references about the applications of vivianite, "particularly in producing high-value products like lithium batteries" (Lu et al., mentioning Wang et al., 2023). Moreover, vivianite "can be efficiently synthesized during the anaerobic fermentation of waste-activated sludge (WAS)". Lu and coworkers concentrate the research on the use of carbonaceous materials in vivianite formation; the researchers mention graphite, carbon nanotubes, and biochar, "as a more affordable, easily produced, and sustainable carbon material, [which] holds significant potential in accelerating electron transfer processes" (Lu et al., and references therein). Therefore, "understanding the vivianite synthesis system's response mechanisms after adding biochar is crucial for improving the efficiency of vivianite formation". About biochar, see Sparavigna, 2023, and references therein.

"As an important product of extracellular electron transfer (EET) and biological iron reduction, the production of vivianite can be enhanced by conductive materials. Carbon nanotubes (CNTs) with excellent electrical conductivity have been reported to promote electron transfer, which was applied in wastewater treatment to accelerate the degradation of the contaminants" (He et al., 2022). He and coworkers studied the influence of carbon nanotubes CNTs in vivianite production. "The enhancement of vivianite production after CNTs adding reached up to 17 % by promoting the electron transfer between dissimilative iron-reducing bacteria (DIRB) and Fe(III)".

Recently, 2024, Li and coworkers "comprehensively investigated the impact and underlying mechanisms of NH_4^+ [ammonium] on the kinetics and product properties of vivianite crystallization for phosphate recovery". As the researchers observe, "high-phosphorus wastewater often contains high concentrations of ammonium".

Vivianite and biochar

Liu et al., 2022, prepared magnetic biochar (MB) "and innovatively applied to enhance P recovery as vivianite. The effects of anaerobic digestion time, hydrothermal pretreatment temperature and MB dose on vivianite formation were investigated using batch experiments and a modified sequential P extraction protocol". According to the researchers, the addition of magnetic biochar, "decreased the proportion of water-extractable P by sorption and promoted organic P decomposition, which further facilitated vivianite production".

Magnetic biochar is also useful in the "phosphorus recovery from waste-activated sludge [WAS] through vivianite crystallization", according to Wu and coworkers, 2023. Actually, "the relatively small crystal size restricts the separation and recovery of vivianite". Wu and coworkers prepared magnetic biochar (MB), "and selected [it] as an additive to enhance vivianite crystallization during WAS anaerobic digestion. The effects of MB iron loading and dosage on the phosphorus recovery efficiency and methane yield were investigated through batch experiments, … The results showed that the phosphorus recovery efficiency reached 45% and the methane yield increased by 27%" under proper conditions. "The microbial analysis found the functional bacteria related to Fe^{3+} reduction and methane production were further enhanced and enriched by the MB". According to the researchers, their study "confirms the feasibility of recovering phosphorus in the form of vivianite from waste-activated sludge using magnetic biochar as the seed crystal, which is conducive to its subsequent separation and utilization" (Wu et al., 2023). Magnetic biochar can be easily collected from water with magnetic fields (Sparavigna, 2023).

"Microbial Fe (III) reduction generally could outcompete methanogenesis due to its thermodynamic advantage, while the low bioavailability of Fe (III) compounds limits this process in the anaerobic digestion system, which could result in the low recovery of vivianite" (Cheng et al., 2023). The study by Cheng and coworkers "investigated the competition between Fe (III) reduction and methanogenesis in the presence of different biochar (pyrochar and hydrochar)".

In 2017, Zhou and coworkers explained that biochar "contains quinones and aromatic structures that facilitate extracellular electron transfer between microbial cells and insoluble minerals". For their study, Zhou et al. prepared granulated biochar and powdered biochar, "amended to two ferrihydrite enrichments to investigate the effect of biochar with different particle sizes on dissimilatory iron(III)-reducing bacteria (DIRB) and methanogens". The researchers concluded that "biochar addition significantly stimulated the reduction of both in situ ferrihydrite and ex situ ferrihydrite and the production of methane". Zhou and coworkers mentioned green rust $Fe_2(CO_3)(OH)$, vivianite $Fe_3(PO_4)_2{\cdot}8(H_2O)$, and iron oxide ($\gamma$-$Fe_2O_3$). They stress that their "study illustrated that the addition of biochar affected iron-reducing and methane-generating microbial communities to some extent".

As a fertilizer

"Vivianite offers a promising way for recovering P from secondary sources such as wastewater sewage sludge, since the efficiency and feasibility of the recovery process have already been proven" (Metz et al. 2023, mentioning Wu et al., 2919, Prot et al.,

2020, Zhang et al., 2022). "The success of vivianite as a recycled P source depends not only on its recovery but also on its reusability, e.g., as a fertilizer. A quantitative understanding of dissolution rates and mechanisms is fundamental to understanding the suitability of vivianite as a P source" (Metz et al., 2023). The researchers find that "the determined dissolution rates of vivianite are fast and exceed the dissolution rates of other common phosphate minerals such as struvite, variscite, or apatite, potentially contributing to its efficiency as a fertilizer" (Metz et al., 2023). Struvite is a magnesium ammonium phosphate ($MgNH_4PO_4{\cdot}6H_20$). Variscite is a hydrated aluminum phosphate mineral ($AlPO_4{\cdot}2H_2O$). Apatite is the name of a group of phosphate minerals. However, Metz and coworker stress that, "in natural soils, vivianite oxidation and the presence of alternative P sinks may impact the solubility. Furthermore, aging effects and especially oxidation might substantially change the properties of vivianite and, consequently, the extent to which P from vivianite becomes bioavailable in soils. Therefore, alkaline calcareous soils may be disadvantageous for vivianite application due to the lower dissolution and faster oxidation kinetics of dissolved Fe(II). The effectiveness of vivianite as a P fertilizer is co-determined by a variety of biogeochemical and hydrological soil processes and conditions. … The mechanistic understanding of anaerobic vivianite dissolution discussed [by Metz and coworker] can serve as a basis for investigating the processes in natural settings. Also, since vivianite is metastable in oxic environments and most agricultural soils are oxic, the impact of oxidation on the dissolution kinetics and solubility of vivianite is of particular interest" (Metz et al., 2023). The term "oxic" is often used to describe an environment where oxygen is present.

From wastewaters to batteries

"Further applications for producing and using the mineral are around the corner", according to www.water4all-partnership.eu. "EU funds like the RECAP project stimulate research in vivianite outside of the wastewater treatment setting, for instance in manure and lake sediments. Using vivianite as fertilizer could be a serious contender in some niche markets. Even more compelling is the fact that vivianite could be a perfect raw material for Lithium Iron Phosphate ($LiFePO_4$ or LFP) batteries, which do not require cobalt".

Biovivianite

The "biovivianite is a potentially useful Fe and P fertilizer, [and therefore] there is much interest in harnessing microbial biovivianite synthesis for circular economy applications". Eshun and coworkers, 2024, study "the factors that influence the formation of microbially-synthesized vivianite (biovivianite) under laboratory batch systems including the presence and absence of phosphate and electron shuttle, the buffer system, pH, and the type of Fe(III)-reducing bacteria (comparing Geobacter sulfurreducens and Shewanella putrefaciens)". "Green rust, a key intermediate in biovivianite production, could be detected as an endpoint alongside vivianite and metavivianite ($Fe^{2+}Fe^{3+}{}_2(PO_4)_2{\cdot}(OH)_2{\cdot}6H_2O$), in treatments with G. sulfurreducens and S. putrefaciens. However, XRD indicated that vivianite abundance was higher in experiments containing G. sulfurreducens, where it dominated" (Eshun et al., 2024).

"Microorganisms can transform phosphorus (P)-enriched iron (Fe)-oxide sludge into products with higher P concentration or can directly promote the precipitation of P-rich compounds from water. However, there is no evidence of these products' efficiency as fertilizers". Further studies by Eshun and coworkers, 2024, investigated biovivianite to assess its effectiveness as P and Fe fertilizer for durum wheat and white lupin. The researchers claim that "the mineral constituents of the biovivianite coupled with their nano-crystallite sizes" explain the vivianite effectiveness as P and Fe fertilizer (Eshun et al., 2024).

Vivianite uses

A description of vivianite traditional uses is given by geologyin.com . Vivianite has scientific uses. It is an *environmental indicator*: "Vivianite's presence in sediments can reveal past environmental conditions, including oxygen levels, pH, and the availability of iron and phosphorus. This information aids in reconstructing paleoclimate and understanding past ecological changes". It is a *geochemical tracer*: "Researchers studying the transportation and fate of iron and phosphorus in aquatic environments can utilize vivianite as a natural tracer due to its specific formation conditions and reactivity". Vivianite is a *paleontological tool*: "Fossilized vivianite alongside fossils of organisms like fish or plants can provide insights into ancient ecosystems and the interactions between organisms and their environment". Besides the scientific uses, we have the use of vivianite as a gemstone and for mineral collection. The web site is also mentioning the vivianite *cultural use*, with associated symbolic values. Moreover, we have vivianite used for pigments, that is, as "vivianite blues" (Slomp, 2023).

Where?

On Earth, as previously told, natural locations to find vivianite are swamps, bogs, wetlands, marshes, and mining areas. "On Mars, even though no positive detection of vivianite has been done, its presence, along with other phosphates, can be expected in patches with high concentration of phosphorus, since other common minerals could mask their existence"

(Silva et al., 2024, mentioning Dyar et al., 2014). However, in Treiman et al., 2023, vivianite is mentioned in a discussion about the manganese-iron phosphate nodules at Gale Crater, Mars. "The MSL Curiosity rover investigated dark, Mn-P-enriched nodules in shallow lacustrine/fluvial sediments at the Groken site in Glen Torridon, Gale Crater, Mars. Applying all relevant information from the rover, the nodules are interpreted as pseudomorphs after original crystals of vivianite, $(Fe^{2+},Mn^{2+})_3(PO_4)_2{\cdot}8H_2O$, that cemented the sediment soon after deposition". Treiman and coworkers affirm that "the most likely such minerals are laueite and strunzite". These minerals "occur on Earth as alteration products of other Mn-bearing phosphates including vivianite". "Vivianite is a common primary and diagenetic precipitate from low-oxygen, P-enriched waters". Available "data suggest that the nodules originated as vivianite" (Treiman et al., 2023).

On Moon? A hydrated mineral, $(NH_4)MgCl_3{\cdot}6H_2O$, has been found in lunar soil samples returned by the Chang'e-5 mission (Jin et al., 2024). Incidentally: "the presence of water and ammonium molecule in ULM-1 crystal are confirmed in both the Raman and Infrared (IR) spectra. The strong normal vibrational modes at 3430 cm^{-1} (symmetric stretching ν_1) and at 1645 cm^{-1} (bending O–H deformations ν_2) of H_2O molecule have been clearly observed in the Raman spectrum of ULM-1" by Jin and coworkers. Note please the importance of the use of Raman broad scans to study the presence of water in minerals.

Vivianite structure

"In pure endmember vivianite all the iron is divalent, Fe^{2+}, but there are two distinct sites in the structure that these ions can occupy. In the first site, the Fe^{2+} is surrounded by four water molecules and two oxygens, making an octahedral group. In the second site, the Fe^{2+} is surrounded by two water molecules and four oxygens, again making an octahedral group. The oxygens are part of the phosphate groups (PO_4^{3-}), that are tetrahedral. The vivianite structure has chains of these octahedra and tetrahedra that form sheets perpendicular to the a-crystal axis. The sheets are held together by weak bonds, and that accounts for the perfect cleavage between them" (Wikipedia, mentioning Pring, 1998).

"Structurally, vivianite belongs to the *C*2/*m* space group. It consists of sheets comprising single (Fe_I) $FeO_2(H_2O)_4$ and double (Fe_{II}) $Fe_2O_4(H_2O)_4$ octahedral sites that are linked by PO_4 tetrahedra (the vivianite crystal is visualized in Figure S1). These sheets are only weakly held together by hydrogen bonds between the H_2O ligands, explaining the perfect cleavage along the 010 plane" (Metz et al., 2023, mentioning Rouzies & Millet, 1993, McCammon & Burns, 1980). "Under oxic conditions, vivianite is unstable, and structural Fe(II) oxidizes rapidly to Fe(III), changing the mineral's appearance ... The oxidation of Fe(II) impacts the crystal structure …" (Metz et al., and references therein).

IR and Raman spectroscopy

Paskin, 2024, tells that infrared and Raman spectroscopy are helpful in vivianite identification. "The IR spectrum of vivianite shows characteristic H-O-H stretching and bending modes at nearly 3430 cm^{-1} and 1690 cm^{-1} respectively, the tetrahedral phosphate group shows vibrations at 974 – 1037 cm^{-1}. … . An advantage of using Raman spectroscopy over IR is that data below 400 cm^{-1} can be obtained. Vivianite shows strong broad O-H stretching bands between 3000 to 3700 cm^{-1} . The strongest band in the Raman spectrum is at 3262 cm^{-1} attributable to the OH stretching. A strong band is observed at 951 cm^{-1} and is due to the Raman active PO stretching. Two intense bands are observed at 236 and 186 cm^{-1} and these bands are attributable to Fe-O stretching vibrations" (Paskin mentioning Frost et al., 2002).

In the article by Frost and coworkers, 2002, we can find the Raman and IR spectra of vivianite, baricite and bobierrite in their Figures 1 and 2. The analysis of the Raman and IR spectra are reported in Table 1 of their article. In the following Table I, we consider only the Raman bands (cm^{-1}), as in the Figure 1 in Frost et al., 2002.

Table I (centers of the bands, cm^{-1})

Vivianite	Baricite	Bobierrite	
3496	3480	3498	Assignment
3482	3300	3263	proposed
3262	3231	3212	
3130	3121	3096	Hydroxyl
3012	3025	2895	stretching

"Vivianite shows well-resolved bands in the hydroxyl-stretching region at 3496, 3482, 3262, 3130 and 3012 cm^{-1}" (Frost et al., 2002). "The band at 3262 cm^{-1} is most intense in the Raman spectrum and is assigned to the water *OH symmetric stretching* mode". "The Raman spectra of both baricite and bobierrite are less well resolved than that of vivianite, although the spectral profiles are similar". The

instrument used by Frost and coworkers is a Renishaw 1000 Raman. The Raman spectra were excited by a He-Ne laser (633 nm). "Repeated acquisitions using the highest magnification were accumulated to improve the signal to noise ratio in the spectra". "Band-component analysis was undertaken using the Jandel 'Peakfit' software package, … Band fitting was done using a Gauss-Lorentz cross-product function with the *minimum number of component bands used to achieve a satisfactory fit*. The Gauss-Lorentz ratio was maintained at values *greater than 0.7*". The Gauss-Lorentz cross product functions are not given in the article by Frost et al.; in Origin Help we find an expression which is governed by parameter "s" as shape. Probably, the "ratio" in Frost et al. is the "shape" in Origin. In the Table I given by Frost and coworkers, four bands are given, but in the Figure 1 of the same article the components used for fitting are five.

In Ogorodova et al., 2017, we can find in their Figure 3 a Raman spectrum of vivianite. "Raman spectroscopic study was carried out on a Raman microscope EnSpectr R532 (Russia) with a diffraction grating (1800 lines/mm) and a spectral resolution of about 6 cm^{-1}. The laser radiation wavelength was equal to 532 nm, the laser radiation power on the sample was approximately 15 mW, … Spectrum was obtained on a non-oriented single crystal". "Anion $[PO_4]^{3-}$ is manifested in the spectrum by a group of lines: a strong line at 950 cm^{-1} corresponds to the totally symmetric valence vibration of the anion; a weak line at 1055 cm^{-1} relates to the triply degenerate antisymmetric valence vibration; the lines at 539 and 572 cm^{-1} belong to the triply degenerate deformation vibration; a line near 458 cm^{-1} corresponds to doubly degenerate deformation vibration of tetrahedra $[PO_4]^{3-}$. The high-frequency line with maximum at 3138 cm^{-1} and shoulder near 3280 cm^{-1} correspond to the valence vibrations of OH-groups (in water molecules). A weak line with maximum near 3475 cm^{-1} relates to valence vibrations of OH-groups in the coordination $Fe^{3+}OH$" (Ogorodova et al., mentioning Frost et al., 2004). In the Figure 3 of the article by Ogorodova et al., we find the peaks at (cm^{-1}): 132, 170, 198, 241, 345, 458, 539, 572, 624, 850, 950, 1055, 1663, 3138, 3280 and 3475.

In the work by Frost et al., 2004, we find the Raman spectra of several samples of vivianite. Again, we find that the researchers used PeakFit and Gauss-Lorentzian cross product functions, "with the minimum number of component bands used for the fitting process". The following table contains the centers of the peaks of natural vivianite samples given by Frost et al. in 2004, plus the centers given in Frost et al., 2002, and those given by Ogorodova et al.

Table II (centers of the bands, cm^{-1})

Chernomorskiy(a)		3137	3268		3487
Blackbird Dist		3131	3247		3473, 3486
Huanuni(a)		3131	3242, 3270, 3272		3480
Monserrat	2958	3133	3262		3478
Chernomorskiy(b)	3031	3137	3253	3351	3493
Huanuni(b)	3010	3135	3257	3391	
Vivianite (2002)	3012	3130	3263		3482, 3496
Ogorodova et al.		3138	3280		3475

We can see that three peaks are always detected. Moreover, the hydroxyl-stretching Raman region seems being composed by five bands in generals.

Frost et al., 2002, wrote that "the band at 3262 cm^{-1} is most intense in the Raman spectrum and is assigned to the water OH symmetric stretching mode". Ogorodova et al., 2017, wrote that "the high-frequency line with maximum at 3138 cm^{-1} and shoulder near 3280 cm^{-1} correspond to the valence vibrations of OH-groups (in water molecules)". Due to these two affirmations, it is necessary to shortly consider the Raman spectrum of water.

Water

In previous discussions, Sparavigna, 2024, we have reviewed literature and proposed the deconvolution of the hydroxyl-stretching region of water and ice with the q-Gaussian functions. For a comparison water/ice we used the Figure 2 in Đuričković et al., 2011. As other researchers did, Đuričković and coworkers noted that the "broad range of the Raman spectrum of liquid water originates from the symmetric and asymmetric OH–stretching vibrations. The fact that this band is rather broad implies the need for its deconvolution into several components, and a large controversy about the number of components and their origins exists in the literature" (Đuričković et al., mentioning Wang et al., 2003). According to the used number of components, researchers established the vibrational mechanisms from intra- and intermolecular bonds (see discussion in Sparavigna, 2024). Let us consider just two components, for instance. We can find them assigned to symmetric and asymmetric vibrations respectively, as in Đuričković et al., 2011. If we use four

components, we can find Carey, 1998, saying that these bands are corresponding to four modes due to "the splitting of the v_1 symmetrical stretching vibration into four distinct vibrations".

In our previous discussion about water and ice, we considered two main q-Gaussian components, characterized by two different q-parameters. We proposed the two parameters as linked to two different local environments of OH-bonds (the q-parameters of q-Gaussians can be related to the correlation time of stochastic Kubo modelling of fluctuations). As stressed by Martin Chaplin in his discussion about the vibrational spectra, the "water structuring is now firmly established … as best interpreted using a two-state water mixture" (Chaplin mentioning Gallo et al., 2016). Of course, the two states have a different local environment for their oscillators.

In Gallo et al., Section 4, we find told that theoretical and experimental results are today modelled by the presence of "two alternative structures" in water, "described as a low- and a high-density liquid". "The anomalies of supercooled water and the possibility of metastable liquid–liquid separation in water can be explained if water is viewed as a mixture of two interconvertible organizations of hydrogen bonds whose ratio is controlled by thermodynamic equilibrium" (Gallo et al., 2016). The water molecules are consequently organized "into two distinct groups: one corresponding to low-energy/low entropy ordered configurations and the other to high-energy/high-entropy configurations. In this picture the complexity of water is thus modeled by a mixture of these two structural motifs" (Gallo et al., 2016).

As previously told, for our deconvolution of the water 3200-3400 cm^{-1} band, we proposed the q-Gaussian functions, which have a shape changing from Lorentzian to Gaussian, according to the q-parameter of the q-exponential Tsallis function (see Appendix). We linked the q-parameter to the local environment of the oscillators. In fact, the approach with q-Gaussians is suitable for a two-fluids model, where each fluid is characterized by a different entropic index (the q-parameter is the entropic index of the Tsallis entropy).

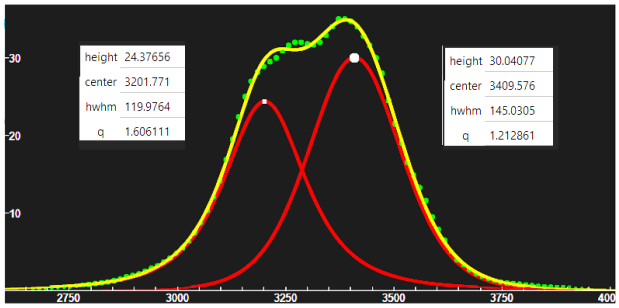

Fig.1: Deconvolution of the OH-stretching band of water, obtained by means of two q-Gaussian functions (red curves). The green dots are representing the data as given in Đuričković et al., 2011. The yellow line is the sum of components. Parameters of the functions are given close the components. Note the different values of the q-parameters (q=1.61 component to the left, q=1.21 component to the right), meaning that oscillators are in two different environments. The plot is obtained by means of software Fityk, after defining in it the q-Gaussian functions (see Appendix for further details).

Let us consider the data from Đuričković et al., 2011, and make a fit with two q-Gaussian functions (Fig.1). We can clearly see that the two q-Gaussians have different q-parameters, and consequently two different Tsallis entropic indexes (again, we can argue that the different entropic indexes are due to two different local environments with two different entropies). We can improve the fit, adding two further small components (Fig.2).

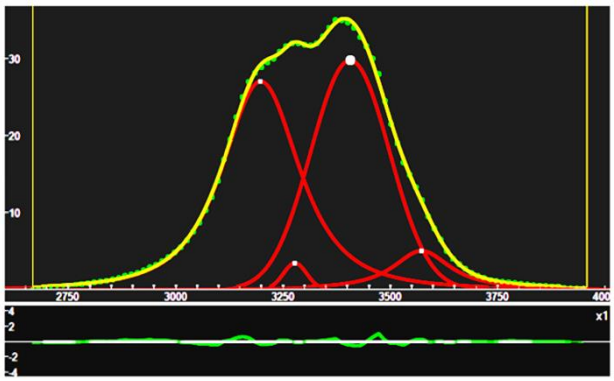

Fig.2: Increasing the number of components the misfit, that is the difference between data and sum of components, given in the lower part of the image is reduced.

After these reminders about water, let us pass to consider the OH-stretching region of vivianite, and to the deconvolution of it. The Raman spectra that we consider are those kindly provided by RRUFF.

RRUFF database

The aim of the RRUFF Project is that of creating "a complete set of high-quality spectral data from well characterized minerals". Moreover, RRUFF "is developing the technology to share this information with the world". Further information about the project is given in Lafuente et al., 2015. In RRUFF we can find several spectra of vivianite. To decompose them, we will use the q-Gaussians. For

what is regarding the number of components, since from literature we can identify five band as in our Table II, let us try deconvolutions with five components.

Vivianite R060025. RRUFF ID: R060025, Ideal Chemistry: $Fe^{2+}_3(PO_4)_2 \cdot 8H_2O$. Locality: Gypsy mine, Minas Gerais, Brazil. Source: Eric Van Valkenburg. Owner: RRUFF. Description: Blue-green fragment. Status: The identification of this mineral has been confirmed by X-ray diffraction. Broad scan on unoriented sample. Instrument settings: Thermo Almega XR 532nm @ 100% of 150mW. We use the processed data, in the range from 2000 to 4000 cm^{-1}. A spline baseline adjustment is applied. The deconvolution is given in the Figure 3.

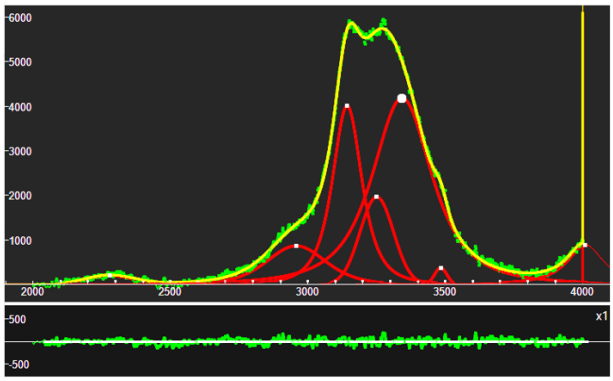

Fig.3: Deconvolution of vivianite RRUFF R060025 spectrum. The OH-stretching region is decomposed into five q-Gaussian bands (red curves). The centers of the components are at 2957, 3143, 3250, 3342, 3483 cm^{-1}.The lower part of the image is showing the misfit, that is the difference between data (green) and the sum of components (yellow curve).

Vivianite R050596. RRUFF ID: R050596. Locality: Chernomorskiy Quarry, near Kertch City, Crimea Peninsula, Ukraine. Source: Barb Dutrow. Owner: RRUFF. Description: Group of dark blue elongated prismatic single crystals in a fossilized clam shell. Status: The identification of this mineral has been confirmed by X-ray diffraction and chemical analysis. Microprobe fragment with measured chemistry: $(Fe^{2+}_{2.89}Mg_{0.08}Mn_{0.03})_{\Sigma=3}(P_{1.00}O_4)_2 \cdot 8H_2O$. Unoriented sample with instrument settings: Thermo Almega XR 532nm @ 100% of 150mW. We use the processed data, in the range from 2000 to 4000 cm^{-1}. A spline baseline adjustment is applied. The deconvolution is given in the Figure 4.

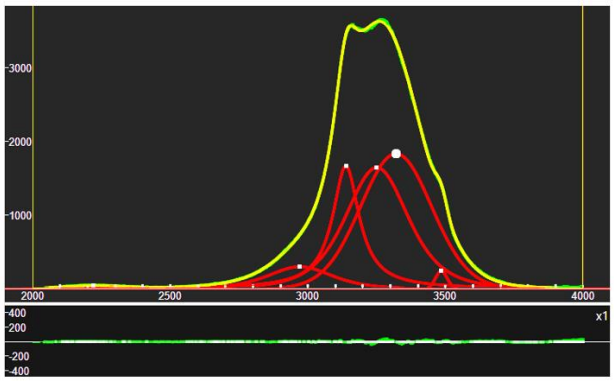

Fig.4: Deconvolution of vivianite RRUFF R050596 spectrum. As in the previous figure, the OH-stretching region is decomposed into five q-Gaussian bands. The centers of the components are at 2971, 3138, 3250, 3320, 3485 cm^{-1}.

Vivianite R050464. Locality: Siglo XX mine, Llallagua, Potosi, Bolivia. Source: University of Arizona Mineral Museum 11555. Owner: RRUFF. Description: Bluish green elongated prismatic crystals. Status: The identification of this mineral is confirmed by single-crystal X-ray diffraction and chemical analysis. Microprobe fragment with measured chemistry: $Fe^{2+}_{3.00}(P_{1.00}O_4)_2 \cdot 8H_2O$. Sample Description: Unoriented sample, Instrument settings: Thermo Almega XR 532nm @ 100% of 150mW. We use the processed data, in the range from 2000 to 4000 cm^{-1}. A spline baseline adjustment is applied. The deconvolution is given in the Figure 5.

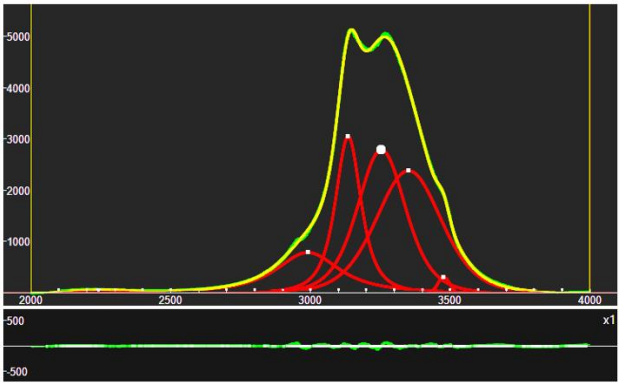

Fig.5: Deconvolution of vivianite RRUFF R050464 spectrum. The centers of the components are at 2990, 3135, 3254, 3351, 3477 cm^{-1}.

Vivianite R050076. Locality: near Canutillos mine, Potosi, Saavedra, Bolivia. Source: Rock Currier. Owner: RRUFF. Description: Green prismatic and elongated single crystal. Status: The identification of this mineral has been confirmed by X-ray diffraction and chemical analysis. Microprobe fragment with measured chemistry: $Fe^{2+}_{0.99}Mn_{0.01})_3(P_{1.00}O_4)_2 \cdot 8H_2O$. Unoriented sample. Instrument settings: Thermo Almega XR 532nm @ 100% of 150mW. We use the raw data, in the range from 2000 to 4000 cm^{-1}. A spline baseline adjustment is applied. The deconvolution is given in the Figure 6.

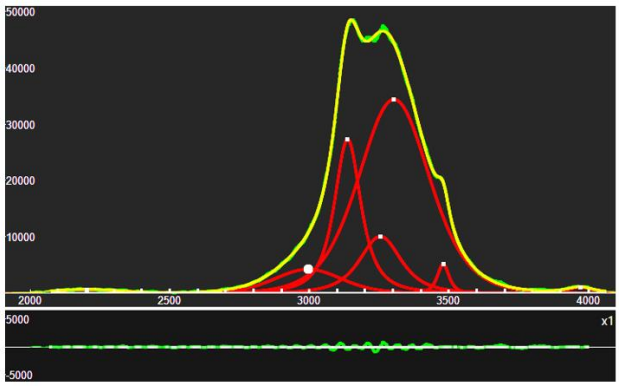

Fig.6: Deconvolution of vivianite RRUFF R050076 spectrum. The centers of the components are at 2996, 3137, 3254, 3303, 3480 cm^{-1}.

Vivianite R040185. Locality: Siglo XX mine, Llallagua, Bustillos, Potosi, Bolivia. Source: University of Arizona Mineral Museum 11555. Owner: RRUFF. Description: Green acicular single crystal. Status: The identification of this mineral has been confirmed by X-ray diffraction and chemical analysis. Microprobe fragment with measured chemistry: $(Fe_{1.00}Mn_{0.01})_3(P_{0.97}Si_{0.03}O_{3.94}F_{0.07})_2 \cdot 8H_2O$. Unoriented sample. Instrument settings: Thermo Almega XR 532nm @ 100% of 150mW. We use the raw data, in the range from 2000 to 4000 cm^{-1}. A spline baseline adjustment is applied. The deconvolution is given in the Figure 7.

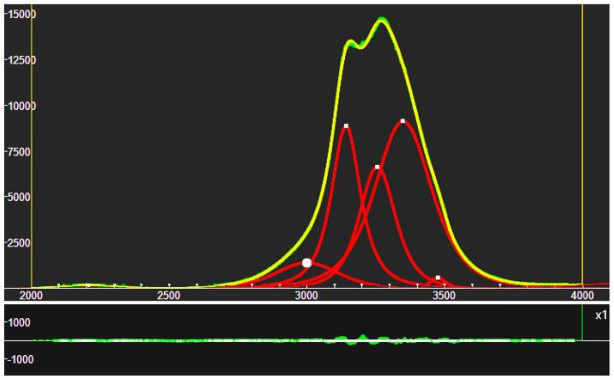

Fig.7: Deconvolution of vivianite RRUFF R040185 spectrum. The centers of the components are at 3000, 3141, 3255, 3349, 3475 cm^{-1}.

Vivianite R070331. Locality: Big Fish River, Yukon Territory, Canada. Source: Mark Mauthner 3369. Owner: RRUFF. Description: Platy, indigo-blue massive, associated with maricite. Status: The identification of this mineral is confirmed by single-crystal X-ray diffraction and chemical analysis. Measured chemistry: $(Fe^{2+}_{1.77}Mg_{1.21}Mn_{0.02})_{\Sigma=3}(P_{1.00}O_4)_2 \cdot 8H_2O$; (dark phase, H_2O is estimated by difference) : $Na_{1.00}Fe^{2+}_{1.00}P_{1.00}O_4$ (light phase = maricite, with trace amounts of Mn). Unoriented sample. Instrument settings: Thermo Almega XR 532nm @ 100% of 150mW. We use the raw data, in the range from 2000 to 4000 cm^{-1}. A spline baseline adjustment is applied. The deconvolution is given in the Figure 8.

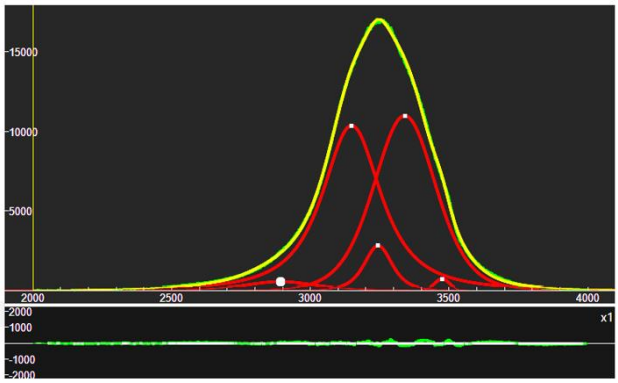

Fig.8: Deconvolution of vivianite RRUFF R070331 spectrum. The centers of the components are at 2892, 3148, 3244, 3340, 3475 cm^{-1}.

Let us pass to other materials of the vivianite group. Baricite R061045. Ideal Chemistry: $(Mg,Fe)_3(PO_4)_2 \cdot 8H_2O$. Locality: Rapid Creek, Yukon, Canada. Source: Michael Scott S100392. Owner: RRUFF. Description: Bluish-gray translucent fragment. Status: The identification of this mineral is confirmed by single-crystal X-ray diffraction and chemical analysis. Microprobe fragment with measured chemistry: $(Mg_{1.66}Fe_{1.33}Mn_{0.01})_{\Sigma=3}(P_{1.00}O_4)_2 \cdot 8H_2O$; H_2O estimated by difference. Unoriented sample. Instrument settings: Thermo Almega XR 532nm @ 100% of 150mW. We use the raw data, in the range from 2000 to 4000 cm^{-1}. A spline baseline adjustment is applied. The deconvolution is given in the Figure 9.

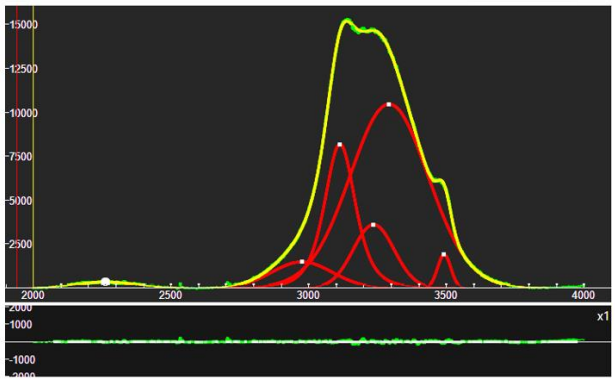

Fig.9: Deconvolution of baricite RRUFF R061045 spectrum. The centers of the components are at 2975, 3113, 3236, 3292, 3492 cm^{-1}.

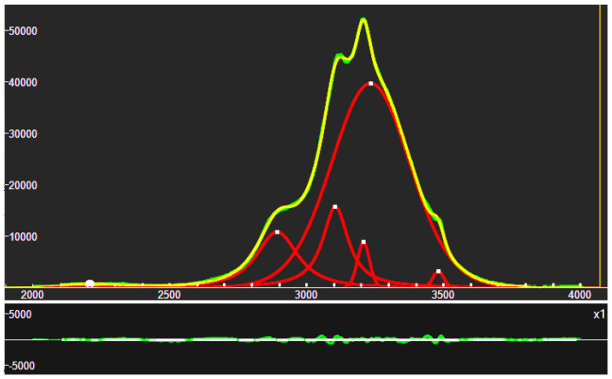

Fig.10: Deconvolution of bobierrite RRUFF R060681 spectrum. The centers of the components are at 2892, 3105, 3207, 3233, 3481 cm^{-1}.

Bobierrite R060681. Ideal Chemistry: $Mg_3(PO_4)_2 \cdot 8H_2O$. Locality: Kovdor Massif, Kola Peninsula, Murmanskaja Oblast', Northern Region, Russia. Source: Michael Scott S101377. Owner: RRUFF. Description: Colorless sectile tabular crystals. Status: The identification of this mineral has been confirmed by X-ray diffraction and chemical analysis. Microprobe Fragment. Measured Chemistry: $(Mg_{2.94}Fe_{0.05}Mn_{0.01})_{\Sigma=3}(P_{1.00}O_4)_2 \cdot 8H_2O$; H_2O estimated by difference. Unoriented sample. Instrument settings: Thermo Almega XR 532nm @ 100% of 150mW. We use the raw data, in the range from 2000 to 4000 cm^{-1}. A spline baseline adjustment is applied. The deconvolution is given in the Figure 10.

In the following Table III, we add the results from RRUFF samples (in cm^{-1}) to those given in the Table III (vivianite).

Table III (centers of the bands, cm^{-1})

R060025	2957	3143	3250	3342	3483
R050596	2971	3138	3250	3320	3485
R050464	2990	3135	3254	3351	3477
R050076	2996	3137	3254	3303	3480
R040185	3000	3141	3255	3349	3475
R070331	2892	3148	3244	3340	3475
Chernomorskiy(a)		3137	3268		3487
Blackbird Dist		3131	3247		3473, 3486
Huanuni(a)		3131	3242, 3270, 3272		3480
Monserrat	2958	3133	3262		3478
Chernomorskiy(b)	3031	3137	3253	3351	3493
Huanuni(b)	3010	3135	3257	3391	
Vivianite (2002)	3012	3130	3263		3482, 3496
Ogorodova et al.		3138	3280		3475

Let us also add to the data of baricite and bobierrite in the Table I the results we obtained on RRUFF samples. The comparison is given in the Table IV.

Table IV (centers of the bands)

Baricite R061045	2975	3113	3236	3292	3492
Baricite (Frost et al.)	3025	3121	3231	3300	3480
Bobierrite R060681	2892	3105	3207	3233	3481
Bobierrite (Frost et al.)	2895	3096	3212	3263	3498
Bobierrite (Ogorodova et al., 2020)		3121	3208		3429, 3439

Discussion – From the Table III and IV, it seems that agreement exists among data. Then, one could ask why to use q-Gaussian functions instead of Gauss-Lorentz cross-product functions. Good reasons exist. First, as we have previously told, the q-parameter of the q-Gaussian is linked to the local environment of the oscillators. This parameter allows the function to assume a shape ranging from Gaussian to Lorentzian. Moreover, what is a Gauss-Lorentz cross product function? We have an expression of it given by Origin. There, we find the shape parameter s; when s is equal to 1, we have a Lorentzian function.

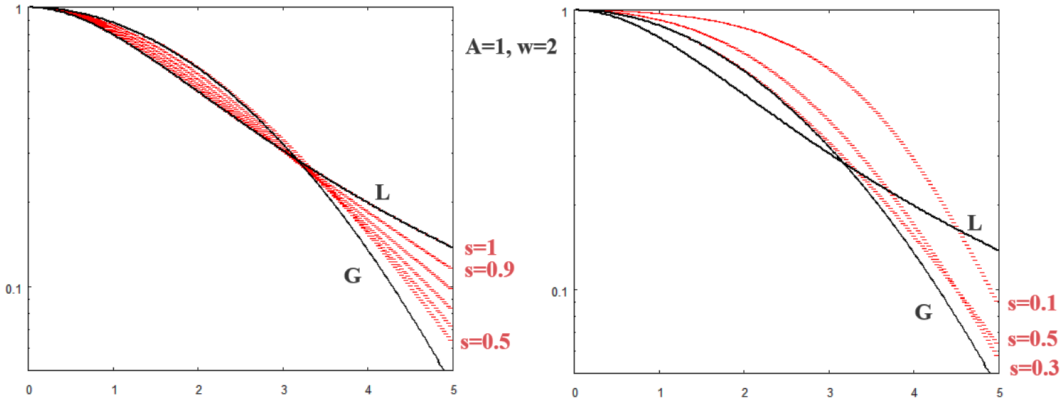

Fig.11: Behavior of the Gauss-Lorentz cross product function as given by Origin, in semilogarithmic scale, with the shape parameter varying from 0.1 to 1. Curves L and G are the Lorentzian and Gaussian functions.

Given the behavior of the Gauss-Lorentz cross product function as in the Fig.11, it is clear why Frost et al. used shape parameters greater than 0.7. It is also clear that a Gaussian shape can be never obtained. Then, let us consider a further Table V, where we show, besides the centers of the band, also their q-parameters.

Table V (centers and q-parameters of the q-Gaussian bands)

R060025	2957, 1.30	3143, 1.59	3250, 0.999	3342, 1.64	3483, 1.001
R050596	2971, 1.41	3138, 2.06	3250, 1.40	3320, 1.05	3485, 0.999
R050464	2990, 1.75	3135, 1.61	3254, 1.31	3351, 1.22	3477, 0.999
R050076	2996, 1.18	3137, 1.68	3254, 1.53	3303, 1.25	3480, 1.56
R040185	3000, 1.21	3141, 1.65	3255, 1.45	3349, 1.42	3475, 0.999
R070331	2892, 1.49	3148, 1.74	3244, 1.47	3340, 1.25	3475, 0.999

The Table V tells us that bands which are far from being Lorentzian are present. This is a good reason for using q-Gaussians, instead of Gauss-Lorentz cross product functions. The q-Gaussians are able to produce line shapes which are close or very close to the Gaussian line shapes.

Other minerals of the vivianite group

The RRUFF database is proposing 17 spectra of minerals of the vivianite group. Six are of vivianite, one of baricite and one of bobierrite. Here in the following, other spectra deconvolutions of minerals among those proposed by RRUFF are given. We propose the spectra where the hydroxyl-stretching region is enough significant.

Annabergite, R050462. Ideal Chemistry: $Ni_3(AsO_4)_2 \cdot 8H_2O$. Locality: Plaka mine, Laurium, Attica, Greece. Source: University of Arizona Mineral Museum 2447. Owner: RRUFF. Description: Green bladed crystals. Status: The identification of this mineral has been confirmed by X-ray diffraction and chemical analysis. Measured Chemistry: $(Ni_{2.97}Zn_{0.03})_{\Sigma=3}(As_{1.00}O_4)_2 \cdot 8H_2O$; lighter vein: $(Ni_{2.95}Zn_{0.05})_{\Sigma=3}(As_{1.00}O_4)_2 \cdot 8H_2O$. Unoriented sample. Instrument settings: Thermo Almega XR 532nm @ 100% of 150mW. We use the processed data, in the range from 2000 to 4000 cm^{-1}. A spline baseline adjustment is applied. The deconvolution is given in the Figure 12.

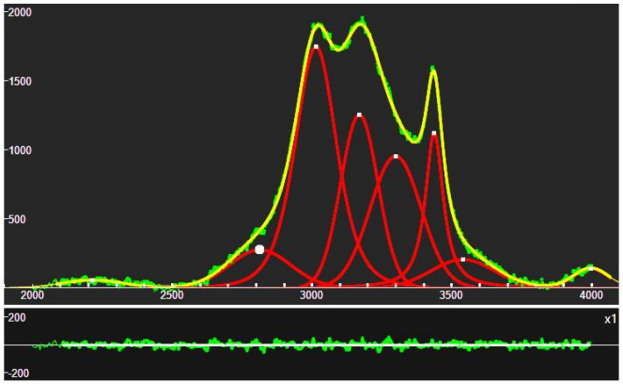

Fig.12: Deconvolution of annabergite RRUFF R050462 spectrum. The centers of the components are at 2805, 3014, 3171, 3302, 3437, 3539 cm^{-1}.

Annabergite R060564. Locality: Candelaria mine, Mineral County, Nevada, USA. Source: Michael Scott S100290. Owner: RRUFF. Description: Aggregates of green thin bladed crystals. Status: The identification of this mineral has been confirmed by single-crystal X-ray diffraction. Unoriented Raman on the primary sample. Instrument settings: Thermo Almega XR 532nm @ 100% of 150mW. We use the raw data, in the range from 2000 to 4000 cm^{-1}. A spline baseline adjustment is applied. The deconvolution is given in the Figure 13.

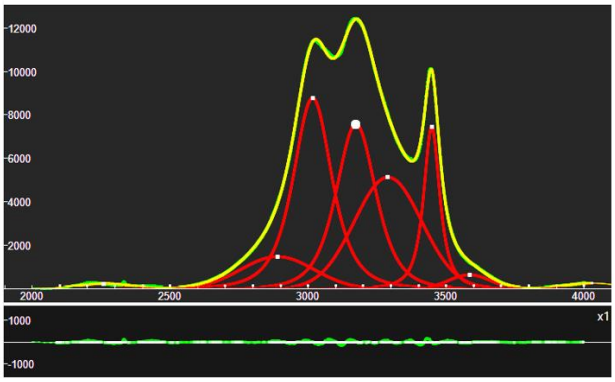

Fig.13: Deconvolution of annabergite RRUFF R060564 spectrum. The centers of the components are at 2888, 3016, 3173, 3289, 3448, 3584 cm^{-1}.

Table VI (annabergite, centers of components, cm^{-1})

R050462	2805	3014	3171	3302	3437	3539
R060564	2888	3016	3173	3289	3448	3584

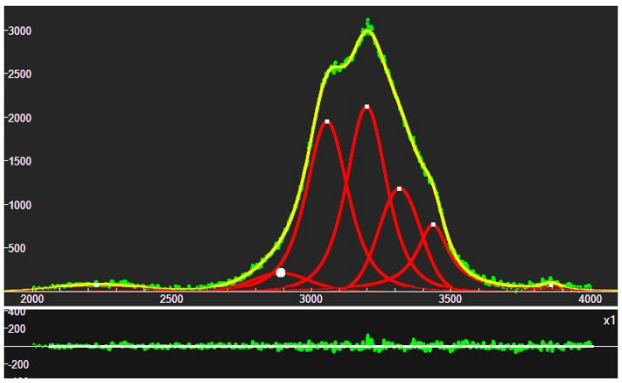

Fig.14: Deconvolution of erythrite RRUFF R050073 spectrum. The centers of the components are at 2889, 3056, 3197, 3316, 3435 cm^{-1}.

Erythrite R050073. Ideal Chemistry: $Co_3(AsO_4)_2 \cdot 8H_2O$. Locality: Bou Azzer, Morocco. Source: Rock Currier. Owner: RRUFF. Description: Crimson flattened crystals. Status: The identification of this mineral has been confirmed by X-ray diffraction and chemical analysis. Sample Description: Microprobe Fragment. Measured Chemistry: $(Co_{0.65}Mg_{0.35})_3(As_{1.00}O_4)_2 \cdot 8H_2O$. Unoriented sample. Instrument settings: Thermo Almega XR 532nm @ 65% of 150mW. We use the raw data, in the range from 2000 to 4000 cm^{-1}. A spline baseline adjustment is applied. The deconvolution is given in the Figure 14.

In Martens et al., 2003, we find told that "four Raman bands are observed in the hydroxyl stretching region of erythrite in the 298 K spectrum, as expected. There are two types of water molecules in the unit cell and consequently there are four OH units, which can vibrate both in-phase and out-of-phase, giving four bands". In the Table 1 in Martens et al. we can find given peaks at 3052, 3200, 3337 cm^{-1} for samples at room temperature. In our Table VII we propose the comparison of data.

Table VII (erythrite, centers of components, cm^{-1})

R050073	2889	3056	3197	3316	3435
Martens et al.		3052	3200	3337	

In this work we have mentioned metavivianite. It is a member of the symplesite group. To the study of this group and other mineral, future works will be devoted.

Appendix – q-Gaussian functions

The q-Gaussian functions are probability distributions proper of the Tsallis statistics (Tsallis, 1988, Hanel et al., 2009). These functions are based on a generalized form of the exponential function, characterized by a continuous real parameter q. When q is going to 1, the q-exponential becomes the usual exponential function. The value q=2, (Naudts, 2009), corresponds to the Cauchy distribution, also known as the Lorentzian distribution; the q-Gaussian function is therefore a generalization of the Lorentzian distribution too. The change of q-parameter is allowing the q-Gaussian function to pass from the Gaussian to the Lorentzian distribution. Sparavigna, 2023, proposed for the first time the use of q-Gaussian function in Raman spectroscopy.

As given by Umarov et al., 2008, the q-Gaussian function is: $f(x) = Ce_q(-\beta x^2)$, where $e_q(.)$ is the q-exponential function and C a scale constant (in the exponent, $\beta = 1/(2\sigma^2)$). The q-exponential has expression: $e_q(u) = [1 + (1-q)u]^{1/(1-q)}$.

In Fityk software, a q-Gaussian function can be

defined in the following manner:
define Qgau(height, center, hwhm, q=1.5) = height*(1+(q-1)*((x-center)/hwhm)^2)^(1/(1-q))
q=1.5 the initial guessed value of the q-parameter. Parameter hwhm is the half width at half maximum of the component. When q=2, the q-Gaussian is a Lorentzian function, that we can find defined in Fityk as:
Lorentzian(height, center, hwhm) = height/(1+((x-center)/hwhm)^2)
When q is close to 1, the q-Gaussian becomes a Gaussian function.

References

1. Carey, D. M., & Korenowski, G. M. (1998). Measurement of the Raman spectrum of liquid water. The Journal of Chemical Physics, 108(7), 2669–2675, https://doi.org/10.1063/1.475659
2. Chaplin, M. (2022). Water structure and science, London South Bank University, https://water.lsbu.ac.uk/water/water_vibrational_spectrum.html
3. Chen, T., Song, X., & Xing, M. (2023). Study on anaerobic phosphorus release from pig manure and phosphorus recovery by vivianite method. Scientific Reports, 13(1), 16095.
4. Cheng, Y., Shi, Z., Shi, Y., Zhang, Y., Zhang, S., & Luo, G. (2023). Biochar promoted microbial iron reduction in competition with methanogenesis in anaerobic digestion. Bioresource Technology, 387, 129561.
5. Đuričković, I., Claverie, R., Bourson, P., Marchetti, M., Chassot, J. M., & Fontana, M. D. (2011). Water–ice phase transition probed by Raman spectroscopy. Journal of Raman Spectroscopy, 42(6), 1408-1412.
6. Dyar, M.D., Jawin, E.R., Breves, E., Marchand, G., Nelms, M., Lane, M.D., Mertzman, S.A., Bish, D.L., & Bishop, J.L. (2014). Mössbauer parameters of iron in phosphate minerals: Implications for interpretation of martian data. American Mineralogist, 99(5-6), pp.914-942.
7. Eshun, L. E., Coker, V. S., Shaw, S., & Lloyd, J. R. (2024). Strategies for optimizing biovivianite production using dissimilatory Fe (III)-reducing bacteria. Environmental Research, 242, 117667.
8. Eshun, L. E., García-López, A. M., Recena, R., Coker, V., Shaw, S., Lloyd, J., & Delgado, A. (2024). Assessing microbially mediated vivianite as a novel phosphorus and iron fertilizer. Chemical and Biological Technologies in Agriculture, 11(1), 47.
9. Frisenda, R., Niu, Y., Gant, P., Muñoz, M., & Castellanos-Gomez, A. (2020). Naturally occurring van der Waals materials. npj 2D Materials and Applications, 4(1), 38.
10. Frost, R. L., Martens, W., Williams, P. A., & Kloprogge, J. T. (2002). Raman and infrared spectroscopic study of the vivianite-group phosphates vivianite, baricite and bobierrite. Mineralogical Magazine, 66(6), 1063-1073.
11. Frost, R., & Weier, M. (2004). Raman spectroscopic study of vivianites of different origins. Neues Jahrbuch fur Mineralogie, Abhandlungen, 10, 445-463.
12. Gallo, P., Amann-Winkel, K., Angell, C.A., Anisimov, M.A., Caupin, F., Chakravarty, C., Lascaris, E., Loerting, T., Panagiotopoulos, A.Z., Russo, J., & Sellberg, J.A. (2016). Water: A tale of two liquids. Chemical reviews, 116(13), pp.7463-7500.
13. Hanel, R., Thurner, S., & Tsallis, C. (2009). Limit distributions of scale-invariant probabilistic models of correlated random variables with the q-Gaussian as an explicit example. The European Physical Journal B, 72(2), 263.
14. He, Z., Chang, J., Feng, Y., Wang, S., Yuan, Q., Liang, D., Liu, J. and Li, N., 2022. Carbon nanotubes accelerates the bio-induced vivianite formation. Science of The Total Environment, 844, p.157060.
15. Jeon, K., Lee, N., Bae, S., Goddard III, W. A., Kim, H., & Lee, W. (2015). Theoretical and experimental studies of the dechlorination mechanism of carbon tetrachloride on a vivianite ferrous phosphate surface. The Journal of Physical Chemistry A, 119(22), 5714-5722.
16. Jin, S., Hao, M., Guo, Z., Yin, B., Ma, Y., Deng, L., Chen, X., Song, Y., Cao, C., Chai, C., & Wei, Q. (2024). Evidence of a hydrated mineral enriched in water and ammonium molecules in the Chang'e-5 lunar sample. Nature Astronomy, pp.1-11.
17. Kappler, A., & Newman, D. K. (2004). Formation of Fe(III)-minerals by Fe(II)-oxidizing photoautotrophic bacteria. Geochim. Cosmochim. Ac. 68, 1217–1226. https://doi.org/10.1016/j.gca.2003.09.006
18. Lafuente, B., Downs, R. T., Yang, H., & Stone, N. (2015). 1. The power of databases: The RRUFF project. In Highlights in mineralogical crystallography (pp. 1-30). De Gruyter (O).
19. Li, S., Quhe, R., Weng, M., Feng, Y., Zuo, Y., Xiao, W., Zheng, J., Lu, J, & Pan, F. (2016). Few-layer Fe3 (PO4) 2· 8H2O: novel H-bonded 2D material and its abnormal electronic properties. The Journal of Physical Chemistry C, 120(46), pp.26278-26283.
20. Li, Q., Chen, J. Q., Wang, M., Liu, X., Liu, X., Wang, J., & Mu, Y. (2024). Ammonium Disrupts Vivianite Crystal Hydration to Enhance Crystallization Rate for Phosphorus Recovery. ACS ES&T Engineering, 4(3), 728-736. Liu, J., Cheng, X., Qi, X., Li, N., Tian, J., Qiu, B., Xu, K., & Qu, D. (2018). Recovery of phosphate from aqueous solutions via vivianite crystallization: Thermodynamics and influence of pH. Chemical Engineering Journal, 349, pp.37-46.
21. Liu, Y., Jin, J., Li, J., Zou, Z., Lei, R., Sun, J., & Xia, J. (2022). Enhanced phosphorus recovery as vivianite from anaerobically digested sewage sludge with magnetic biochar addition. Sustainability, 14(14), 8690.
22. Lu, S., Zeng, W., Gong, Q., Zhang, J., Peng, X., Yu, X., & Peng, Y. (2024). Anaerobic recovery of vivianite from waste-activated sludge through combined sludge pre-fermentation and agroforestry biomass-based biochar. Process Safety and Environmental Protection.
23. Martens, W., Frost, R. L., & Kloprogge, J. T. (2003). Raman spectroscopy of synthetic erythrite, partially dehydrated erythrite and hydrothermally synthesized dehydrated erythrite. Journal of Raman Spectroscopy, 34(1), 90-95.
24. McCammon, C. A., & Burns, R. G. (1980). The oxidation mechanism of vivianite as studies by Möessbauer spectroscopy. American Mineralogist, 65(3-4), 361-366.
25. Metz, R., Kumar, N., Schenkeveld, W. D., & Kraemer, S. M. (2023). Rates and Mechanism of Vivianite Dissolution under Anoxic Conditions. Environmental Science & Technology, 57(45), 17266-17277.
26. Miot, J., Benzerara, K., Morin, G., Kappler, A., Bernard, S., Obst, M., Férard, C., Skouri-Panet, F., Guigner, J.M., Posth, N., & Galvez, M. (2009). Iron biomineralization by anaerobic neutrophilic iron-oxidizing bacteria. Geochimica et Cosmochimica Acta, 73(3), pp.696-711.
27. Naudts, J. (2009). The q-exponential family in statistical physics. Central European Journal of Physics, 7, 405-413.
28. Ogorodova, L., Vigasina, M., Mel'chakova, L., Rusakov, V., Kosova, D., Ksenofontov, D., & Bryzgalov, I. (2017). Enthalpy of formation of natural hydrous iron phosphate: Vivianite. The Journal of Chemical Thermodynamics, 110, 193-200.
29. Ogorodova, L. P., Gritsenko, Y. D., Vigasina, M. F., Kosova, D. A., Melchakova, L. V., & Fomina, A. D. (2020). Natural Magnesium hydrous orthophosphates bobierrite and kovdorskite: FTIR, Raman, thermal, and thermochemical study. Geochemistry International, 58, 189-199.
30. Paskin, A. (2024). Nucleation, Growth and Transformation Phenomena of Vivianite (Doctoral dissertation). Doctoral_Dissertation_FU_Berlin
31. Pinto, H. P., Michalkova, A., & Leszczynski, J. (2014). First-principles studies of paramagnetic vivianite Fe3 (PO4) 2· 8H2O surfaces. The Journal of Physical Chemistry C, 118(12), 6110-6121.

32. Priambodo, R., Shih, Y. J., & Huang, Y. H. (2017). Phosphorus recovery as ferrous phosphate (vivianite) from wastewater produced in manufacture of thin film transistor-liquid crystal displays (TFT-LCD) by a fluidized bed crystallizer (FBC). RSC advances, 7(65), 40819-40828.
33. Pring, A. (1998). Dana's New Mineralogy, xiv+ 1819 pp. New York, Chichester, Weinheim, Brisbane, Singapore, Toronto: John Wiley & Sons, Inc. Price£ 190.00 (hard covers). ISBN 0 471 19310 0. Geological Magazine, 135(5), 723-732.
34. Prot, T., Nguyen, V.H., Wilfert, P., Dugulan, A.I., Goubitz, K., De Ridder, D.J., Korving, L., Rem, P., Bouderbala, A., Witkamp, G.J., & Van Loosdrecht, M.C.M. (2019). Magnetic separation and characterization of vivianite from digested sewage sludge. Separation and Purification Technology, 224, pp.564-579.
35. Prot, T., Wijdeveld, W., Eshun, L. E., Dugulan, A. I., Goubitz, K., Korving, L., & Van Loosdrecht, M. C. M. (2020). Full-scale increased iron dosage to stimulate the formation of vivianite and its recovery from digested sewage sludge. Water Research, 182, 115911.
36. Prot, T., Korving, L., Dugulan, A. I., Goubitz, K., & Van Loosdrecht, M. C. M. (2021). Vivianite scaling in wastewater treatment plants: Occurrence, formation mechanisms and mitigation solutions. Water Research, 197, 117045.
37. Rothe, M., Kleeberg, A., & Hupfer, M. (1026). The occurrence, identification and environmental relevance of vivianite in waterlogged soils and aquatic sediments. Earth-Sci. Rev. 158, 51–64. https://doi.org/10.1016/j.earscirev.2016.04.008
38. Rouzies, D., & Millet, J. M. M. (1993). Mössbauer study of synthetic oxidized vivianite at room temperature. Hyperfine Interactions, 77(1), 19-28.
39. Silva, G. G., Vincenzi, R. A., de Araujo, G. G., Venceslau, S. J. S., & Rodrigues, F. (2024). Siderite and vivianite as energy sources for the extreme acidophilic bacterium Acidithiobacillus ferrooxidans in the context of mars habitability. Scientific Reports, 14(1), 14885.
40. Slomp, C.P. (2023). Vivianite blues. Nat. Geosci. 16, 394. https://doi.org/10.1038/s41561-023-01174-7
41. Sparavigna, A. C. (2023). q-Gaussian Tsallis Line Shapes and Raman Spectral Bands. Int. J. Sciences, 12(3), 27-40.
42. Sparavigna, A. C. (2023). q-Gaussian Tsallis Line Shapes for Raman Spectroscopy (June 7, 2023). SSRN Electronic Journal. http://dx.doi.org/10.2139/ssrn.4445044
43. Sparavigna A. C. (2023). Tsallis q-Gaussian function as fitting lineshape for Graphite Raman bands. ChemRxiv. Cambridge: Cambridge Open Engage; 2023.
44. Sparavigna, A. C. (2023). SERS Spectral Bands of LCysteine, Cysteamine and Homocysteine Fitted by Tsallis qGaussian Functions. International Journal of Sciences, 12(09), 14–24. https://doi.org/10.18483/ijsci.2721
45. Sparavigna, A. C. (2023). Multifunctional porosity in biochar. Int. J. Sciences, 7, 41-54. Available https://papers.ssrn.com/sol3/papers.cfm?abstract_id=4544693
46. Sparavigna, A. C. (2023). The Catcher in the Water: Magnetic Biochar for the Treatment of Wastewater. Available at SSRN 4409849.
47. Sparavigna, A. C. (2024). Kubo Lineshape and its Fitted q-Gaussian Tsallis Function. International Journal of Sciences, 13(01), 1-9.
48. Sparavigna, A. C. (2024). Water, q-Gaussians and Raman Spectroscopy. International Journal of Sciences, 13(03), 17-25. http://dx.doi.org/10.18483/ijSci.2751
49. Sparavigna, A. C. (2024). Applying q-Gaussians to the OH-stretching Raman bands of Water and Ice. International Journal of Sciences, 13(04), 1-10. http://dx.doi.org/10.18483/ijSci.2756
50. Treiman, A.H., Lanza, N.L., VanBommel, S., Berger, J., Wiens, R., Bristow, T., Johnson, J., Rice, M., Hart, R., McAdam, A. and Gasda, P., 2023. Manganese-Iron Phosphate Nodules at the Groken Site, Gale Crater, Mars. Minerals, 13(9), p.1122.
51. Tsallis, C. (1988). Possible generalization of Boltzmann-Gibbs statistics. Journal of statistical physics, 52, 479-487.
52. Umarov, S., Tsallis, C., Steinberg, S. (2008). On a q-Central Limit Theorem Consistent with Nonextensive Statistical Mechanics. Milan J. Math. Birkhauser Verlag. 76: 307–328. doi:10.1007/s00032-008-0087-y. S2CID 55967725.
53. Wang, Z., Pakoulev, A., Pang, Y., & Dlott, D. D. (2003). Vibrational substructure in the OH stretching band of water. Chemical physics letters, 378(3-4), 281-288.
54. Wang, S., An, J., Wan, Y., Du, Q., Wang, X., Cheng, X., Li, N. (2018). Phosphorus competition in bioinduced vivianite recovery from wastewater. Environmental science & technology, 52(23), pp.13863-13870.
55. Wang, P., Zuo, W., Zhu, W., Wang, S., Li, B., Jiang, Y., Wang, G., Tian, Y., & Zhang, Y. (2023). Deciphering the interaction of heavy metals with Geobacter-induced vivianite recovery from wastewater. Water Research, 245, p.120621.
56. Wilfert, P., Mandalidis, A., Dugulan, A.I., Goubitz, K., Korving, L., Temmink, H., Witkamp, G.J., & Van Loosdrecht, M.C.M. (2016). Vivianite as an important iron phosphate precipitate in sewage treatment plants. Water research, 104, pp.449-460.
57. Wilfert, P., Dugulan, A. I., Goubitz, K., Korving, L., Witkamp, G. J., & Van Loosdrecht, M. C. M. (2018). Vivianite as the main phosphate mineral in digested sewage sludge and its role for phosphate recovery. Water research, 144, 312-321.
58. Wojdyr, M. (2010). Fityk: a general-purpose peak fitting program. Journal of applied crystallography, 43(5), 1126-1128.
59. Wu, Y., Luo, J., Zhang, Q., Aleem, M., Fang, F., Xue, Z., & Cao, J. (2019). Potentials and challenges of phosphorus recovery as vivianite from wastewater: A review. Chemosphere, 226, 246-258.
60. Wu, Z., Zheng, Q., Zhang, Y., Pang, Y., Huang, T., & Peng, D. (2023). Phosphorus recovery from waste-activated sludge through vivianite crystallization enhanced by magnetic biochar. Journal of Cleaner Production, 392, 136294.
61. Yang, X., Zhang, C., Zhang, X., Deng, S., Cheng, X., & Waite, T. D. (2023). Phosphate recovery from aqueous solutions via vivianite crystallization: Interference of FeII oxidation at different DO concentrations and pHs. Environmental Science & Technology, 57(5), 2105-2117.
62. Zhang, J., Chen, Z., Liu, Y., Wei, W., & Ni, B. J. (2022). Phosphorus recovery from wastewater and sewage sludge as vivianite. Journal of Cleaner Production, 370, 133439.
63. Zhao, L., Liu, L., Liu, X., Shu, A., Zou, W., Wang, Z., Zhou, Y., Huang, C., Zhai, Y. and He, H., 2024. Efficient phosphorus recovery from waste activated sludge: pretreatment with natural deep eutectic solvent and recovery as vivianite. Water Research, p.122161.
64. Zhou, G.W., Yang, X.R., Marshall, C.W., Li, H., Zheng, B.X., Yan, Y., Su, J.Q., & Zhu, Y.G. (2017). Biochar addition increases the rates of dissimilatory iron reduction and methanogenesis in ferrihydrite enrichments. Frontiers in microbiology, 8, p.589.